Combined experimental and numerical study of uniaxial compression failure of hardened cement paste at micrometre length scale

Zhang, Hongzhi; Xu, Yading; Gan, Yidong; Chang, Ze; Schlangen, Erik; Šavija, Branko

DOI
10.1016/j.cemconres.2019.105925

Publication date
2019

Document Version
Final published version

Published in
Cement and Concrete Research

Citation (APA)
Zhang, H., Xu, Y., Gan, Y., Chang, Z., Schlangen, E., & Šavija, B. (2019). Combined experimental and numerical study of uniaxial compression failure of hardened cement paste at micrometre length scale. *Cement and Concrete Research*, *126*, Article 105925. https://doi.org/10.1016/j.cemconres.2019.105925

Cement and Concrete Research 126 (2019) 105925

Contents lists available at ScienceDirect

Cement and Concrete Research

journal homepage: www.elsevier.com/locate/cemconres

Combined experimental and numerical study of uniaxial compression failure of hardened cement paste at micrometre length scale

Hongzhi Zhang[a,b], Yading Xu[b,*], Yidong Gan[b], Ze Chang[b], Erik Schlangen[b], Branko Šavija[b]

[a] School of Qilu Transportation, Shandong University, 250002 Jinan, PR China
[b] Microlab, Faculty of Civil Engineering and Geoscience, Delft University of Technology, 2628 CN Delft, the Netherlands

ARTICLE INFO

Keywords:
Hardened cement paste
Compressive strength
Micromechanics
Nanoindenter
Lattice modelling

ABSTRACT

The aim of this work is to investigate the mechanical performance of hardened cement paste (HCP) under compression at the micrometre length scale. In order to achieve this, both experimental and numerical approaches were applied. In the experimental part, micrometre sized HCP specimens were fabricated and subjected to uniaxial compression by a flat end tip using nanoindenter. During the test, the load-displacement curves can be obtained. In the modelling part, virtual micrometre sized specimens were created from digital material structures obtained by X-ray computed tomography. A computational compression test was then performed on these virtual specimens by a discrete lattice fracture model using the local mechanical properties calibrated in the authors' previous work. A good agreement is found between the experimental and numerical results. The approach proposed in this work forms a general framework for testing and modelling the compression behaviour of cementitious material at the micrometre length scale.

1. Introduction

Cement paste is the binder in concrete that glues aggregates together. Understanding the mechanical properties of cement paste is of great importance for proper designing and improving the performance of concrete. A well-known fact is that concrete is a complex heterogeneous material with heterogeneities ranging from a few nanometres to metres [1]. Furthermore, concrete exhibits different mechanical properties at different length scales [2]. Consequently, fracture modelling and testing should be carried out at every length scale.

During the past decades, most efforts are put on understanding the fracture performance of such material at centimetre length scale in which the specimens can be easily produced and tested with well-controlled boundary conditions. With respect to the compressive failure, which is one of the most studied loading cases in the field of cementitious materials, the measurement and understanding at the micrometre length scale is still missing. With recent advances in multi-scale modelling, the micromechanical properties of cement paste under uniaxial compression are modelled [3–5], showing much higher strength compared with the macroscopic results [6]. Unfortunately, these findings have not been experimentally validated so far. Therefore, the aim of this work is to develop an approach to conduct the uniaxial compression test on cement paste at the micrometre length scale.

Recently, the authors have developed a procedure for producing 100 μm-sized hardened cement paste (HCP) cubes [7]. This approach involves thin-sectioning, polishing and micro-dicing, from which an array of HCP microcubes on a glass substrate can be obtained. This offers an unprecedented opportunity for experimental investigation of compressive failure performance of HCP at the micrometre length-scale. Another possibility would be to use focused ion beam (FIB) milling, which is a common technique for preparation of small sized specimens [8]. This technique uses a finely focused Ga-ion beam for precise micromachining of various materials. However, considering the relatively low milling efficiency, the size of the machined specimen is generally limited up to 10 μm, which is not large enough to represent the HCP matrix but for a single phase in the matrix. Loading of these micrometre sized specimens is generally applied using a nanoindenter. Most common tests include the micro-pillar compression [9] and micro cantilever bending tests [10,11]. In this work, the nanoindenter was adopted as well. A flat end tip was mounted on the nanoindenter instrument to apply a uniformly distributed compressive load.

In order to explain fracture process of HCP during the experiment, a discrete lattice model was used to simulate the uniaxial compression test. This model is one of the most popular to explain fracture in quasi-brittle materials [12,13], mainly because of the predicted realistic crack pattern, relatively simple constitutive relations and failure modes used (commonly, the purely elastic-brittle fracture behaviour is assumed for individual lattice elements), and a straightforward implementation of

* Corresponding author.
E-mail address: Y.Xu-5@tudelft.nl (Y. Xu).

https://doi.org/10.1016/j.cemconres.2019.105925
Received 7 February 2019; Received in revised form 19 August 2019; Accepted 21 October 2019

the material heterogeneity at various levels of observation [14–17]. At micrometre length scale, cement paste is generally regarded as a composite material consisting of several phases: anhydrous cement particles, calcium hydroxide (CH), high-density and low-density calcium-silicate-hydrates (C-S-H) which are also known as inner and outer hydration products, respectively [18,19]. This heterogenous and multiphase microstructure can be obtained either by modelling (e.g. Hymostruc [20], μic [21] and CemHyd3D [22]) or experiments (e.g. X-ray microcomputed tomography [23–25] and Backscattered electron imaging [26,27] for 3D and 2D, respectively). In this research, an X-ray microcomputed tomography (XCT) generated microstructure was used. The elastic-brittle fracture behaviour of local phases is derived from the authors' previous work [16] in which microcubes of the same size were ruptured using a Berkovich tip and the experimentally measured load displacement curves were further used for input calibration. The model was first validated by the experimental measurements and further applied for the prediction of the compressive failure of HCP at the microscale. It is believed that with the presented experimental measuring and numerical modelling, improved insight of the compressive failure performance of HCP at the micrometre scale is provided.

2. Experimental

2.1. Materials

Three cement pastes with different water to cement (w/c) ratios (0.3, 0.4 and 0.5) were used in the current study. They were made by mixing ordinary Portland cement (CEM I 42.5 N) and deionized water with the designed w/c ratio. The pastes were mixed according to EN 196-3:2005 + A1:2008 (E) using a Hobart mixer. First, the cement clinkers were placed in a bowl. Water was added within 10 s. This was followed by mixing for 90 s at low speed. The mixer was then stopped for 30 s during which all paste adhering to the wall and the bottom part of the bowl was scrapped using a metal scraper and added to the mix. The mixing was then resumed for additional 90 s. The total mixer running time was around 3 min. After mixing, fresh mixtures were poured into cylindrical plastic moulds (diameter: 24 mm; height: 39 mm) and compacted on a vibration table to remove air bubbles. Afterwards, the cylinders were sealed and rotated with a speed of 2.5 rpm for 24 h to prevent bleeding. The cement pastes were cured under sealed conditions in lab conditions (temperature: 22 ± 2 °C) for 28 days. The HCP was then demoulded and cut into 2 mm slices using a precision saw. Before further sample preparation and mechanical testing, hydration of hardened HCP was terminated by means of solvent exchange using isopropanol [28]. In this approach, slices were immersed into the solution and taken out five times for a period of 1 min prior to be stored in the solution. After 3 days immersion, the slices were taken out to enable the solvent to evaporate.

2.2. Micrometre sized specimen preparation

Three types of micrometre sized specimens were prepared for HCP with each w/c ratio: two types of micro-cubes with size of 100 μm and 200 μm, and one prism with the height of 400 μm and cross-section of 200 μm × 200 μm. With these three types of specimens, the influence of specimen's size and slenderness ratio, respectively, on the measured micromechanical properties could be investigated. Specimen preparation was performed as follows: first, a slice was bound to a glass substrate using an ultraviolet light (UV) resin (Araldite 2020). In this process, a bonding jig was used to offer constant pressure during UV curing (8 N) and a spike pad was placed in between the slice and jig to improve the uniformity of pressure provided by the jig. In this way, the thickness of adhesive layer (AL) between slice and substrate can be controlled. The thickness of the AL, h_{LA}, is estimated by measuring the total height of specimen before and after bonded to the glass substrate using a length gauge (Heidenhain MT25). It was measured from 6 specimens that $h_{LA} = 18.72 \pm 1.23$ μm (average ± standard deviation).

Afterwards, a thin sectioning process was conducted to prepare HCP slices with a desired thickness (i.e., 400 μm, 200 μm or 100 μm respectively). The slice was ground down to the desired thickness by diamond ring grinding discs with grit size of 125 μm and 30 μm in descending order. Special attention was paid to ensure that two ends of the slice remain smooth: the slice was first ground down to 1 mm thickness, detached, flipped over and bonded to glass substrate again for subsequent grinding.

After thin sectioning, samples were polished with diamond paste (6 μm, 3 μm, 1 μm, and 0.25 μm) on a lapping table in descending order. 15 min was used for each grit size, except the final one which required 30 min of polishing. Specimens were soaked into an ultrasonic bath to remove residue after each polishing step.

The last step was to create the micrometre sized specimens by running a precision micro dicing saw in two perpendicular directions over the slice. The saw is originally used in the microchip industry, by which the material can be diced, grooved or slotted to high tolerances down to 5 μm. This precision cutting makes it suitable for preparing specimens with size of a few hundred micrometres. The distance between every two paralleled cuts was set as the sum of the length of the designed cross-section and the thickness of dicing blade (260 μm). To ensure that also the glue between HCP and glass was sliced, the saw was set to cut a few micrometres into the glass substrate. A grid of micro cubes (or prisms) was formed on the glass substrate in the end. The dimension and quality of the prepared specimens were checked using an environmental scanning electron microscope (ESEM) before the compression test (see Fig. 1).

2.3. Uniaxial compression test

Herein, a KLA-Tencor G200 nanoindenter was used to conduct the uniaxial compression test on the prepared micrometre sized specimens. A diamond flat end tip with a diameter of 330 μm (Fig. 2) was mounted on the XP head to apply a uniformly distributed load on the top surface of the specimen as schematically shown in Fig. 3. The diameter of the tip allows an overall cover of the specimens' surface but avoids touching the other pillar during the test. To ensure only normal force is transmitted to the specimen, the tip was aligned with the centre of the specimen. The positioning accuracy was ensured by aligning the indenter to microscope through an indenter to microscope calibration procedure prior to the test. The compression test was applied to each specimen under load control with a constant loading increment i.e. 10 mN/s. The indenter drift tolerance was set as 0.5 nm. Prior to the experiments, the indenter was calibrated against a fused silica standard. A typical load-displacement curve of the compression test is shown in Fig. 4. It is evident that three stages can be distinguished. In the first stage, the load increases monotonically until reaching a critical load P_c. A nonlinear behaviour is observed at the beginning of the test because of the following sources: unstable contact at the beginning of the test because of small oscillations of the tip, gradually increasing contact between the tip surface and the specimen, and the non-linear deformation of the soft adhesive layer. After regime I, a rapid burst of displacement is observed in the second stage, which indicates that catastrophic failure of the specimen occurs. As the test is performed under load control, the indenter overshoots towards the substrate until it hits the crushed specimen or substrate and continues to load to the prescribed maximum load which is required by the test method. Furthermore, non-linear behaviour is observed just prior to catastrophic failure. This allows a forecast for the catastrophic failure. In order to visualise the cracked specimen prior to the failure, the test was manually terminated in several cases when the aforementioned behaviour was observed. Note that this procedure was only performed for several specimens for image acquiring. The critical load P_c was used to calculate the compressive strength f_c of test specimens:

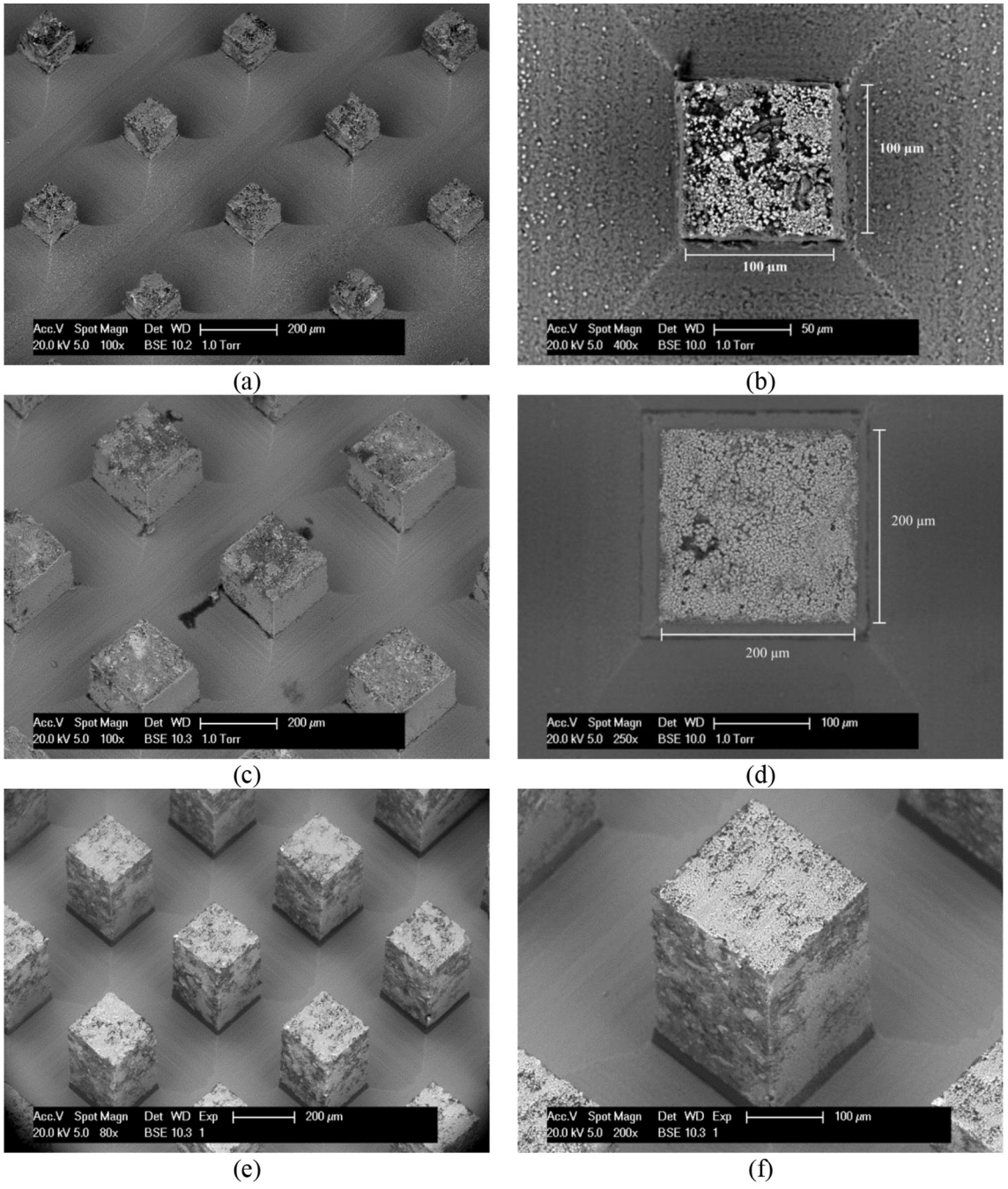

Fig. 1. ESEM images of the fabricated micrometre sized HCP specimens: (a) an array of 100 μm-sized HCP cubes; (b) top view of one 100 μm-sized HCP cube with dimensions; (c) an array of 200 μm-sized HCP cubes; (d) top view of one 200 μm-sized HCP cube with dimensions; (e) an array of HCP prisms with 400 μm height and 200 μm square cross-section; (f) a zoomed-in image of one prism on the glass substrate.

$$f_c = \frac{P_c}{d^2} \tag{1}$$

where d is the dimension of the square cross-section. Young's modulus was determined by the slope in the range between 50% and 80% of the critical load. It is calculated as:

$$E_m = S\frac{h_m}{d^2} \tag{2}$$

where S is the average slope; h_m is the height of specimen measured by the length gauge. Note that the E_m directly derived from the load-displacement curve cannot be used to represent the elasticity of the HCP as the recorded displacement includes also the deformation from the underlying materials (AL and glass substrate) which should be eliminated for evaluation of the stiffness of the HCP. Compared with the AL, the glass substrate has a limited contribution to the measured displacement. If it is assumed that all the materials behave linear-elastic in this region, the following equation can be obtained:

$$\frac{h_m}{E_m} = \frac{h_c}{E_c} + \frac{h_{AL}}{E_{AL}} \tag{3}$$

where h_r is the real height of the specimen and $h_c = h_m - h_{AL}$. E_c is the Young's modulus of the HCP; E_{AL} represents the elastic modulus of the AL. This equation was used in Section 4.1 to calculate the Young's modulus of tested HCP specimens.

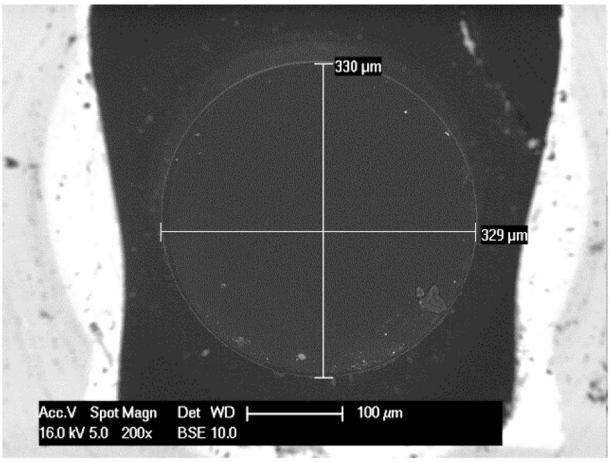

Fig. 2. Top view of the diamond flat end tip with 330 μm in diameter.

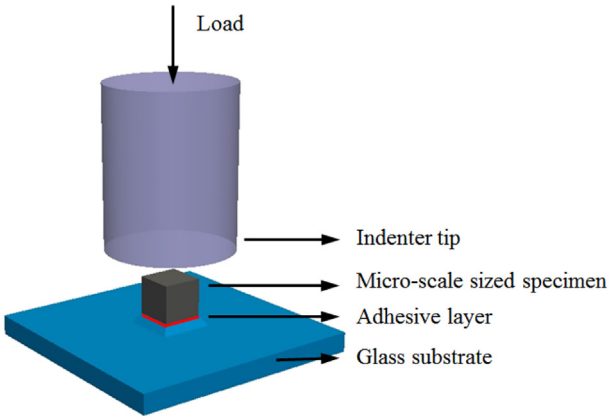

Fig. 3. Schematic illustration of compression test instrumented by the nanoindenter.

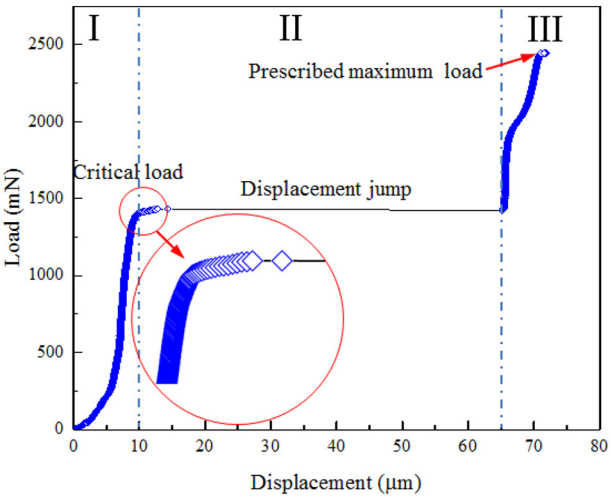

Fig. 4. A typical load-displacement curve of the load-controlled compression test.

3. Modelling

3.1. Digital specimens

At the micrometre length scale, a microstructure containing multiple phases can be observed for HCP [27]. To properly model its micromechanical properties, a multi-phase microstructure should be considered. Herein, an XCT generated microstructure as presented in the authors' previous work [16] was used. Briefly, the grey-scale level CT images with a resolution of 2 μm × 2 μm × 2 μm were obtained by scanning an HCP prism with a cubic cross-section of 400 μm × 400 μm using an XCT scanner. In order to study the influence of w/c ratio on the predicted mechanical properties, three prisms with varying initial w/c ratio 0.3, 0.4 and 0.5 were prepared and scanned. An image thresholding process was then implemented to segment 4 phases from these images, namely: capillary pore (CP), inner hydration product (IHP), outer hydration product (OHP) and anhydrous cement paste (ACP). For more details on the segmentation procedure, the reader is referred to the authors' previous work [16]. Detailed information of segmented microstructure is presented in Table 1. Clearly, with the initial w/c ratio increasing, a higher porosity and hydration degree can be obtained, while a lower amount of anhydrous cement grains remains in the matrix. On the base of the segmented microstructure, two types of virtual specimens were created with respect to each w/c ratio mixture. The first is one having a cubic shape with size of 100 μm × 100 μm × 100 μm which was extracted from the segmented microstructure (Fig. 5). The second one is formed by replacing the volume at bottom up to 20 μm by the adhesive layer (AL) that occurs in the experiments (Fig. 6). This allows a comparison between experimental measurements and numerical modelling.

Table 1
Details of segmented microstructures after [29].

w/c	CP (%)	ACP (%)	Hydration degree (%)
0.3	8.44	15.30	69.65
0.4	11.84	10.64	74.99
0.5	17.50	8.02	80.85

3.2. Deformation and fracture model

Discrete lattice fracture model has been widely used to simulate deformation and fracture in quasi-brittle materials, e.g. cement-based material [14,15,17] and nuclear graphite [30,31], because of its efficiency and simplicity [32]. The model consists of a network of small beams and failure is introduced by removing beams exceeding a local fracture criterion. Heterogeneity of the observed system is considered by introducing spatial distributions of the mechanical properties of local elements. This can be achieved by using either a statistical distribution [33] or a specific material structure (i.e., a voxel based material structure [34]).

The network (Fig. 7a) was generated as follows. First, the spatial domain was divided into a grid of cubic cells. Then, a sub-cell was defined in the centre of each cell. A node was positioned randomly within each sub-cell. Node connectivity is determined by performing a Delaunay triangulation of the domain with respect to the defined nodes, wherein nodes in adjacent Voronoi cells are connected with lattice elements [35]. It is worth mentioning that the ratio between the sub-cell and the cell size controls the degree of randomness of the lattice system. The choice of randomness is important for the fracture analysis, as it has been observed that the simulated crack shape is affected by the orientation of meshes [36]. In order to introduce geometry disorder of material texture and avoid big variations in length of elements, a randomness of 0.5 was adopted herein. Considering the low aspect ratio (length/diameter, averaging 1.2) of the local beam element, a Timoshenko beam element is used to take shear deformation into account [32].

The material heterogeneity was implemented as schematically shown in Fig. 7b. A voxel value was assigned to each node in the lattice mesh based on the material structure used. This was then used to define properties of each lattice element which were made dependent on the

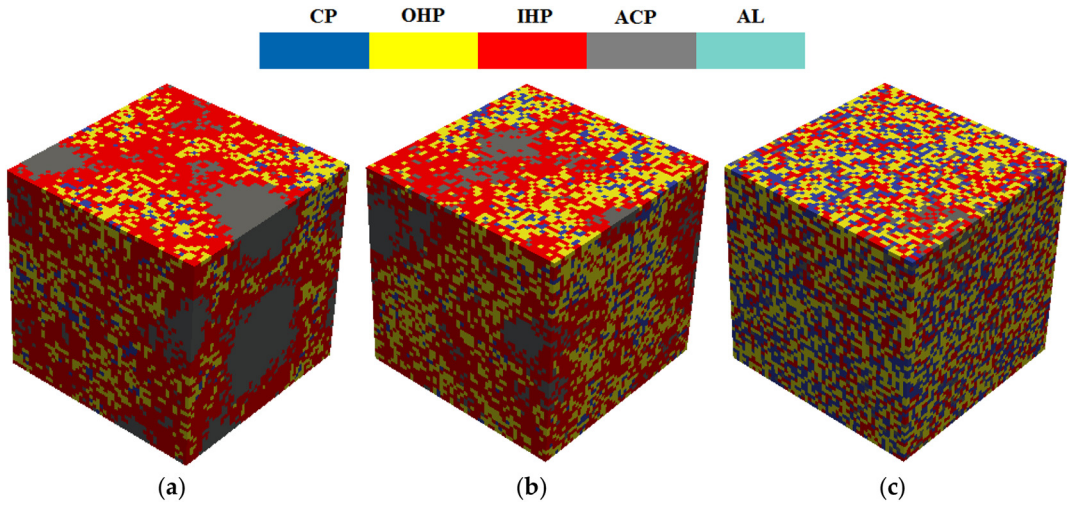

Fig. 5. 3D cubic specimen (100 μm × 100 μm × 100 μm) of HCPs with w/c ratio (a) 0.3; (b) 0.4; (c) 0.5.

pixel-voxel value of its end nodes. Different mechanical properties can be assigned to different phases in the material following the aforementioned approach. The elastic modulus of a lattice element i-j connecting phase i and j was determined using a Reuss model as [37]:

$$\frac{2}{E_{ij}} = \frac{1}{E_i} + \frac{1}{E_j} \tag{4}$$

where E_i and E_j are elastic moduli corresponding to phase i and j, respectively. Note that if either voxel *i* or voxel *j* is a pore voxel, no element is created representing the initial defect in the system. The strength (both compressive and tensile strength) of the lattice element *i-j* was assumed as the lower value in between phases *i* and *j*. In terms of the solid phases that has been explicitly segmented in the HCP microstructures, their elastic moduli were taken from nanoindentation experiments [19]. Their tensile strengths were taken from Ref. [16], in which a micro scale experiment is developed to calibrate these values. These values have also been adopted by the authors for modelling of micro HCP cube under one-sided splitting test [7] and beam under 3-point bending [34]. The modelling results show good agreements with their corresponding micro scale experimental tests. Therefore, these parameters were constantly adopted in the current work. The compressive strength of each phase was then assumed as 10 times higher than the tensile strength considering the fact that cementitious materials have a higher resistance to the compressive loading than tensile [1]. In terms of LA, its elastic modulus is measured by the nanoindentation test [7]. Elements that connect LA phase maintain linear elastic during the simulation.

The compressive boundary conditions were then applied as shown in Fig. 8. In each analysis step, displacement was applied on the one end and the other end was clamped. A set of linear elastic analyses was then performed by calculating the stress within each lattice element as:

$$\sigma = \frac{N}{A} + \alpha_M \frac{\max(M_X, M_Y)}{W} \tag{5}$$

where A is cross-sectional area of the element; W is the second moment of cross-sectional area; α_M is the bending influence factor. On the one hand, for a system that fails under tension, a small value (i.e. 0.05) is generally adopted mainly because of the fact that all beam elements fail in pure mode-I crack [38]. On the other hand, in case of the compression test, the failure process is a combination of several fracture mechanisms, thus a large α_M (i.e. 0.5) is recommended in order to depict the failure introduced by bending [39,40]. In order to keep the model parameters consistent, the α_M is taken as 0.05 when the local lattice element is under tension, while 0.5 is adopted for the compressed elements. In every analysis step, only one element with the highest stress/strength ratio is marked. This is followed by one of the two actions: 1) if it is the first time that a beam element is marked, it degrades from a Timoshenko beam element into a truss element for which only the axial stiffness remains (see Fig. 9); 2) if it is the second time that an element is marked in a subsequent calculation (using the same failure criteria),

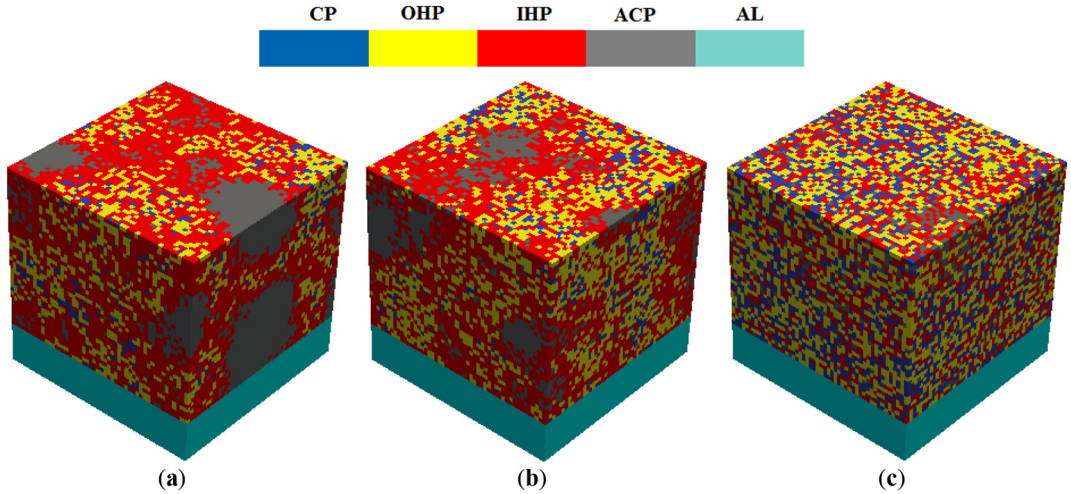

Fig. 6. 3D cubic specimen (100 μm × 100 μm × 100 μm) of HCPs considering adhesive layer (AL) with w/c ratio (a) 0.3; (b) 0.4; (c) 0.5.

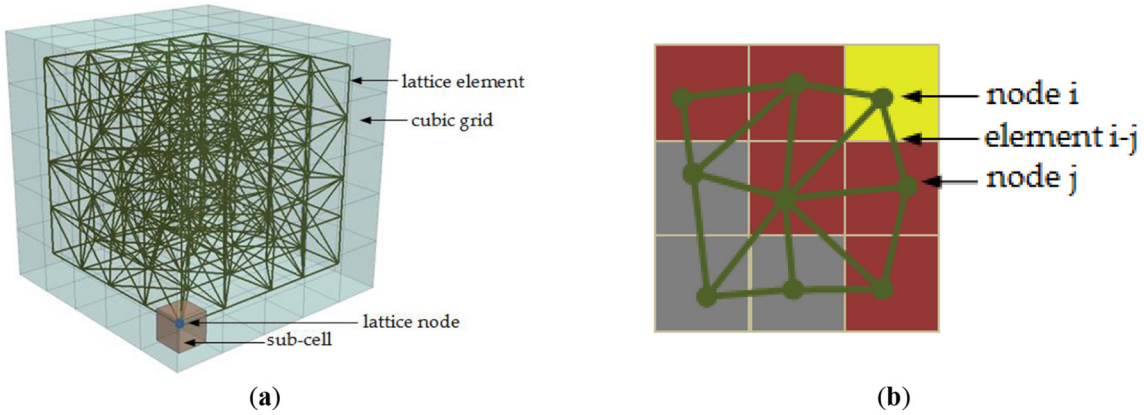

Fig. 7. Schematic view of lattice model generation: (a) Node and mesh generation procedure (5 × 5 × 5); (b) an example of the overlay procedure for HCP, shown in 2D for simplicity, after [16].

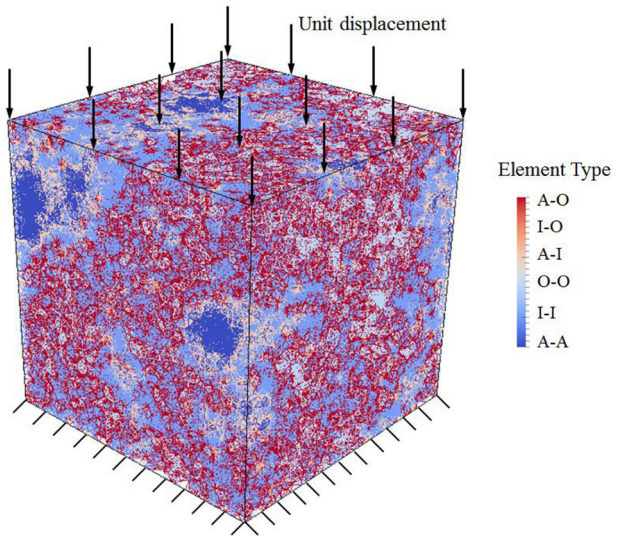

Fig. 8. An example of boundary conditions used for uniaxial compression modelling.

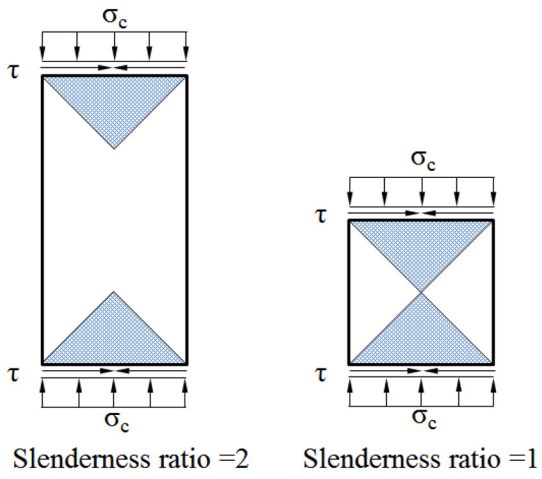

Fig. 10. Confined zones due to frictional restraint for specimens of different slenderness.

the truss element is removed and a small crack is introduced. The second step simulates the friction of crack faces in a way. Note that in order to avoid the overlapping of the neighbouring nodes and to account for the sliding that happened in between the two surfaces of a crack, the truss element was allowed to fail only in tension. The mesh is then updated and relaxed. The calculation procedure is repeated until a predefined stopping criterion (in terms of, e.g., load or displacement) is met.

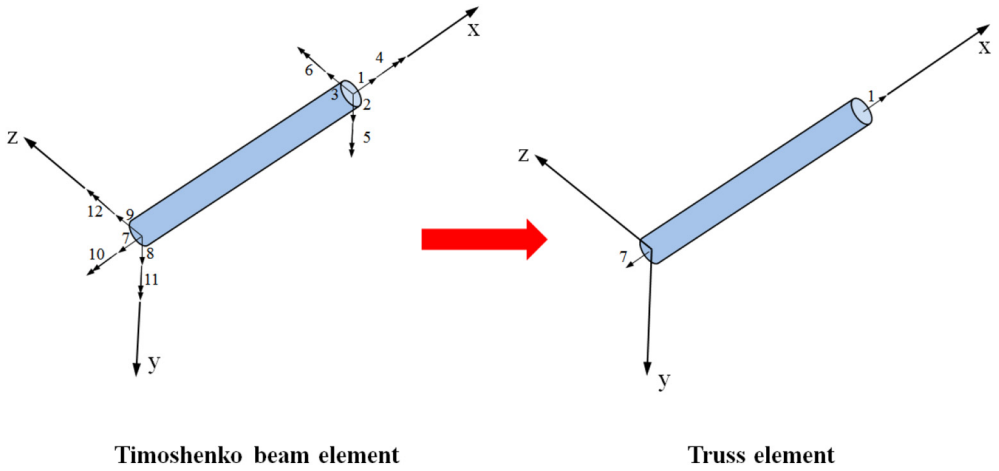

Fig. 9. Schematic view of the element degradation at first step.

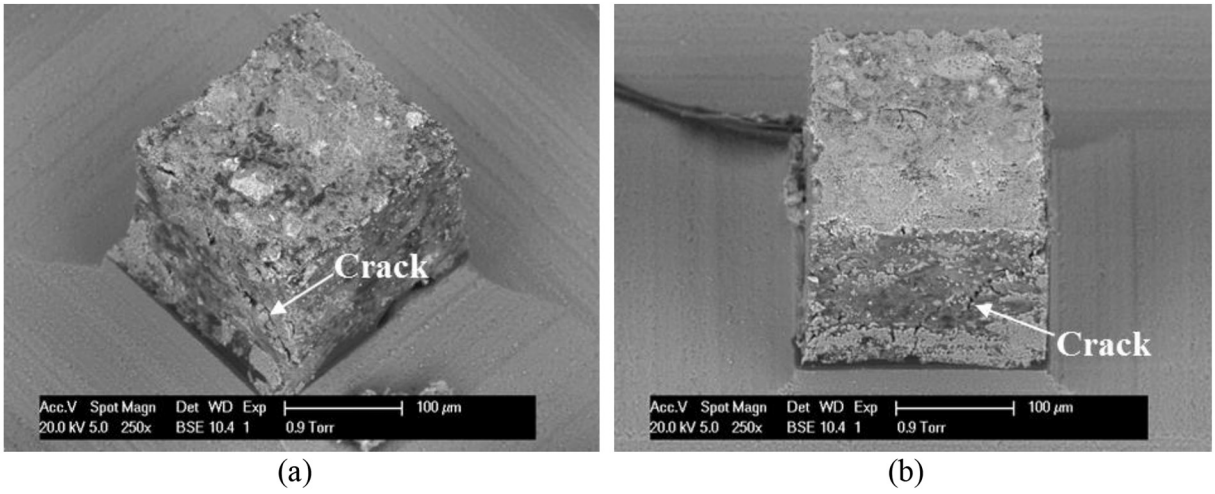

Fig. 11. Characteristic fracture patterns of cubic specimens prior to the catastrophic failure.

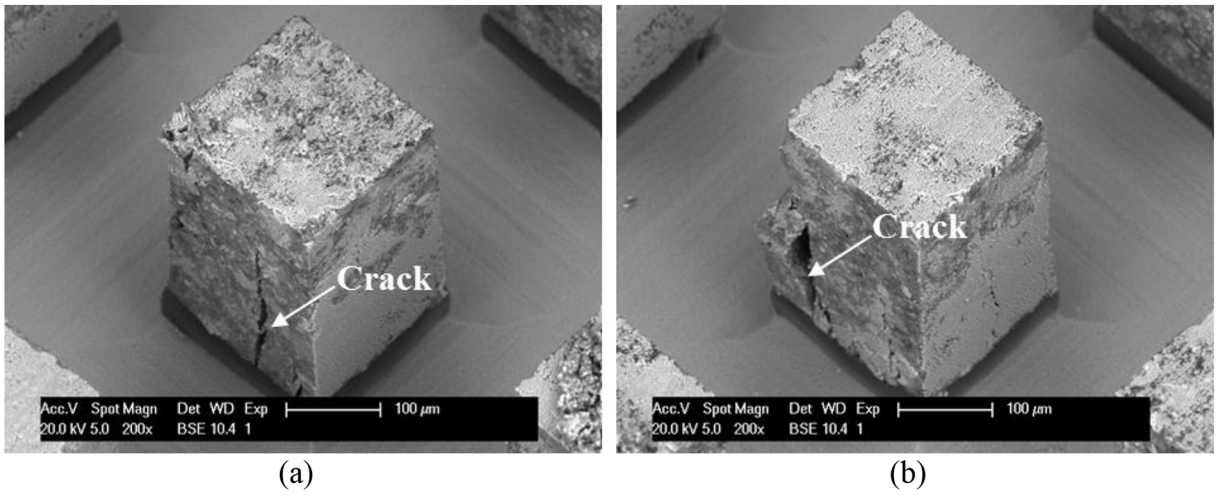

Fig. 12. Characteristic fracture patterns of prismatic specimens prior to the catastrophic failure.

4. Results and discussion

4.1. Experimental results and discussion

Considering the heterogeneity of HCP and its influence on the deformation and fracture performance at the micrometre length scale, for each type specimen, > 100 specimens were produced and tested. Table 3 summaries the calculated strength and elastic modulus using Eqs. (1) and (3). The number in the parentheses is the variation coefficient. From this table, the following trends can be observed:

As expected, for the same type of specimen, the mean value of compressive strength decreases with the initial w/c ratio, while its coefficient of variation increases. The same trend was observed for the elastic modulus. This is mainly because of the fact that a mixture with a higher w/c ratio always has a more porous and heterogeneous microstructure [29]. Note that the compressive strength is measured at equal age, not at equal degree of hydration, for the three w/c ratios (see Table 1).

The size of specimens influences the measured compressive strength and elastic modulus. The smaller cubes have a higher strength and elastic modulus compared with the larger cubes, as large defects (i.e. capillary pores > 100 μm) are not sampled in the smaller specimen. Compared with the elasticity, the size effect has more influence on the strength, since strength is more sensitive to defects compared to elastic stiffness [29].

Cubic specimens have higher strength compared with prismatic specimens of the same cross section, which have a slenderness ratio of 2. As a rigid flat end indenter was used for loading and the bottom of the specimen is fixed on the glass substrate, a relatively high frictional restrained boundary condition is expected for the current uniaxial compression test, although the bottom is less confined compared to the top of the specimen because of the low stiffness of the AL. As explained in the literature [39,41–43], a shear stress between the loading platen and the specimen occurs because of the mismatch in their lateral expansion and stiffness. Consequently, an area of triaxial compression occurs due to confinement at the two ends of the specimen as schematically shown in Fig. 10. It is evident that a specimen with small slenderness has a larger relative restrained area. Thus, a higher strength is expected to be measured from a low slenderness specimen mainly because cementitious material has higher resistance to the triaxial compressive stress than the uniaxial compressive stress. Unlike the compressive strength, the measured elastic moduli are less influenced by the slenderness of specimens as shown in Table 3. Fracture patterns of specimens prior to the catastrophic failure (Figs. 11 and 12) were captured as mentioned in Section 2.3. Clearly, because of the restraint on the ends of the specimen, different crack patterns are observed. For cubic specimens, typically, an hourglass-shape main crack is formed. On the other hand, more straight and vertical cracks are observed for the slenderer specimens.

As more than one hundred specimens were tested for each specimen

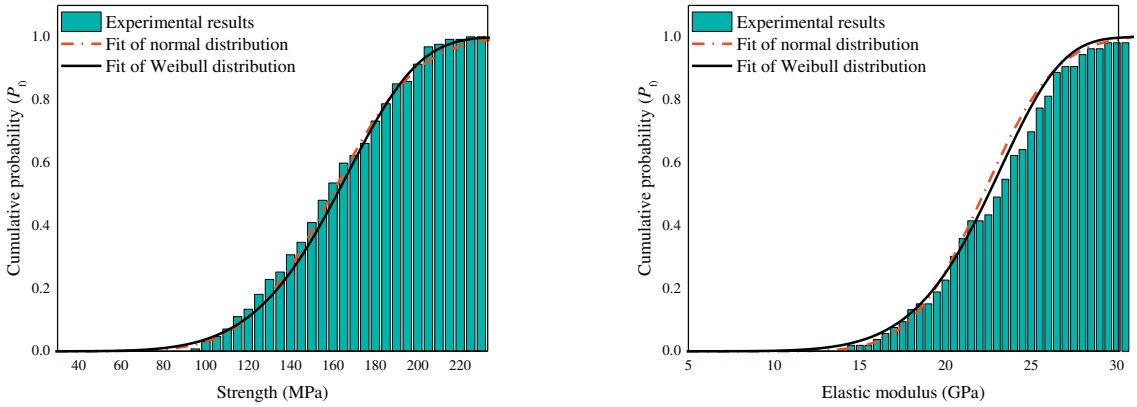

(a)

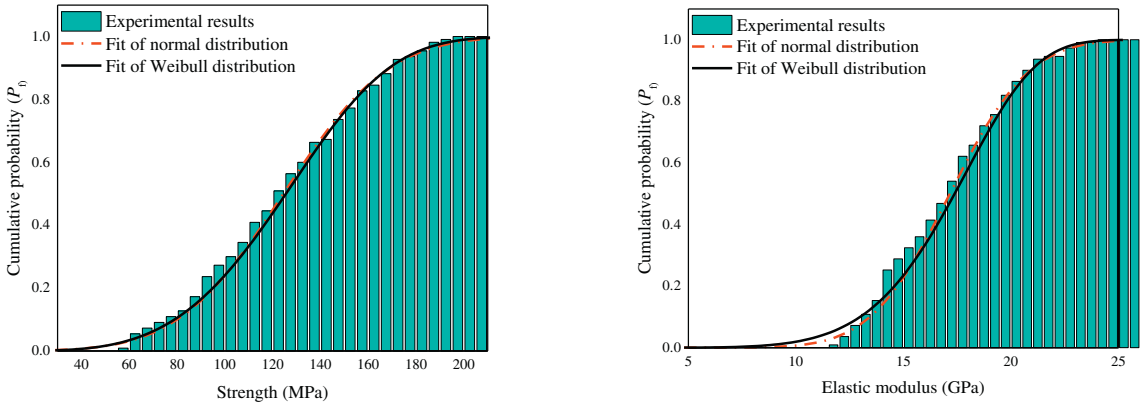

(b)

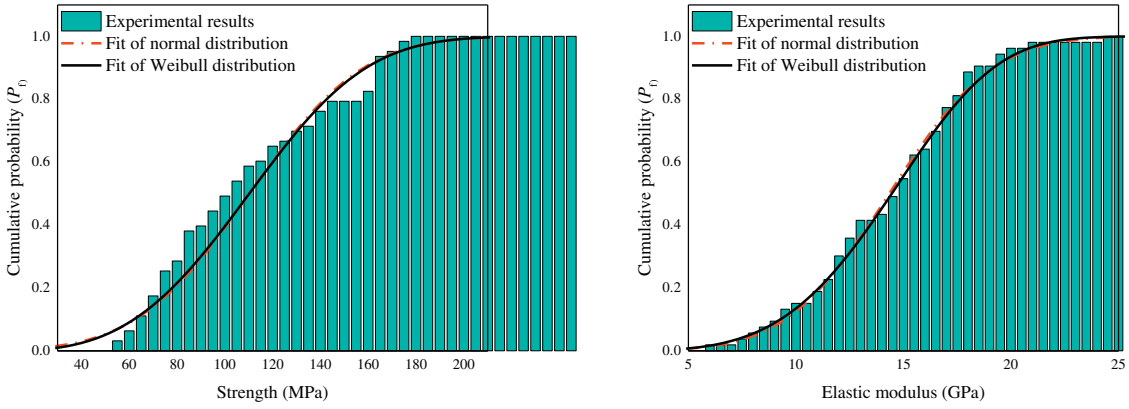

(c)

Fig. 13. Cumulative probability of 100 μm-sized HCP cube with w/c ratio of (a) 0.3, (b) 0.4 and (c) 0.5 (left: strength; right: elastic modulus).

type, it was possible to analyse the measured micromechanical properties statistically. For cementitious materials, normal distribution and two-parameter Weibull statistics are commonly used to describe the statistical distribution of mechanical properties. Their applicability for the micromechanical properties were investigated using the data from the 100 μm cubes. As construction of the experimental probability density function largely depends on the choice of the bin size which would further disturb the fitting results, approach considering the

Table 2
Assigned local mechanical properties of individual phases at micro metre length scale.

Phase	Young's modulus (GPa)	Tensile strength (MPa)	Compressive strength (MPa)
AHC	99 [19]	683 [16]	6830
INP	31 [19]	92 [16]	920
OHP	25 [19]	58 [16]	580
LA	3 [7]	–	–

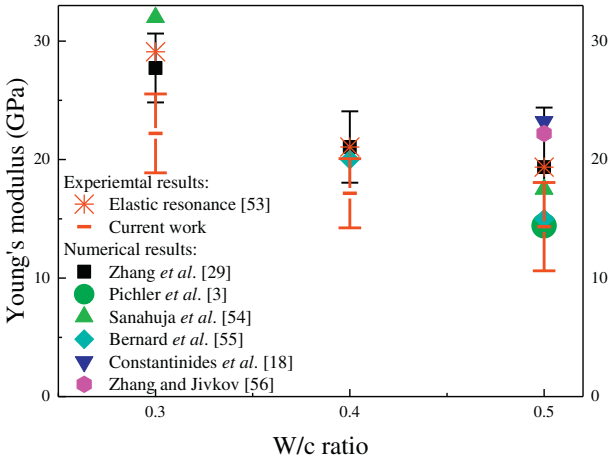

Fig. 14. Comparison of elastic moduli reported in the literature.

cumulative distribution function (CDF) was adopted. The CDF of a normal distribution can be written as [44]:

$$F(x) = \Phi\left(\frac{x-\mu}{s}\right), \tag{6}$$

where μ is the mean value, s is the standard deviation, and Φ is the error function. For the two-parameter Weibull distribution, its CDF are given by [44]:

$$F(x) = 1 - \exp\left[\left(\frac{x}{\eta}\right)^m\right], \tag{7}$$

where m is the shape parameter (also known as Weibull modulus); η is the scale parameter which is defined as the value at the 63.2% percentile. Note that the Weibull distribution is derived from a weakest link theory [45], and has been widely applied for characterisation the strength of brittle or quasi-brittle materials, e.g. concrete [44,46], rocks [47] and ceramics [48]. As the purpose of this study is to see whether these two distributions can be applied for the measured mechanical properties, these two distribution functions were used to fit both experimental measured elastic modulus and compressive strength. The fitting results are shown in Fig. 13. It is observed that, the theoretical CDF curves from different probability functions are closer to each other. The goodness of fitting was checked by a Chi-square goodness-of-fit test. This test determines if a data sample comes from a specified probability distribution. The test groups the data into bins and calculates the observed and expected counts for those bins, and computes the chi-square test statistic [49]:

$$\chi^2 = \sum_{i=1}^{N} (Oi - Ei)^2/E_i \tag{8}$$

where O_i are the observed counts and E_i are the expected counts based on the hypothesized distribution. The test statistic has an approximate chi-square distribution when the counts are sufficiently large. The fitting results are listed in Tables 4 and 5 for normal distribution and Weibull distribution, respectively. It is shown that, for all three

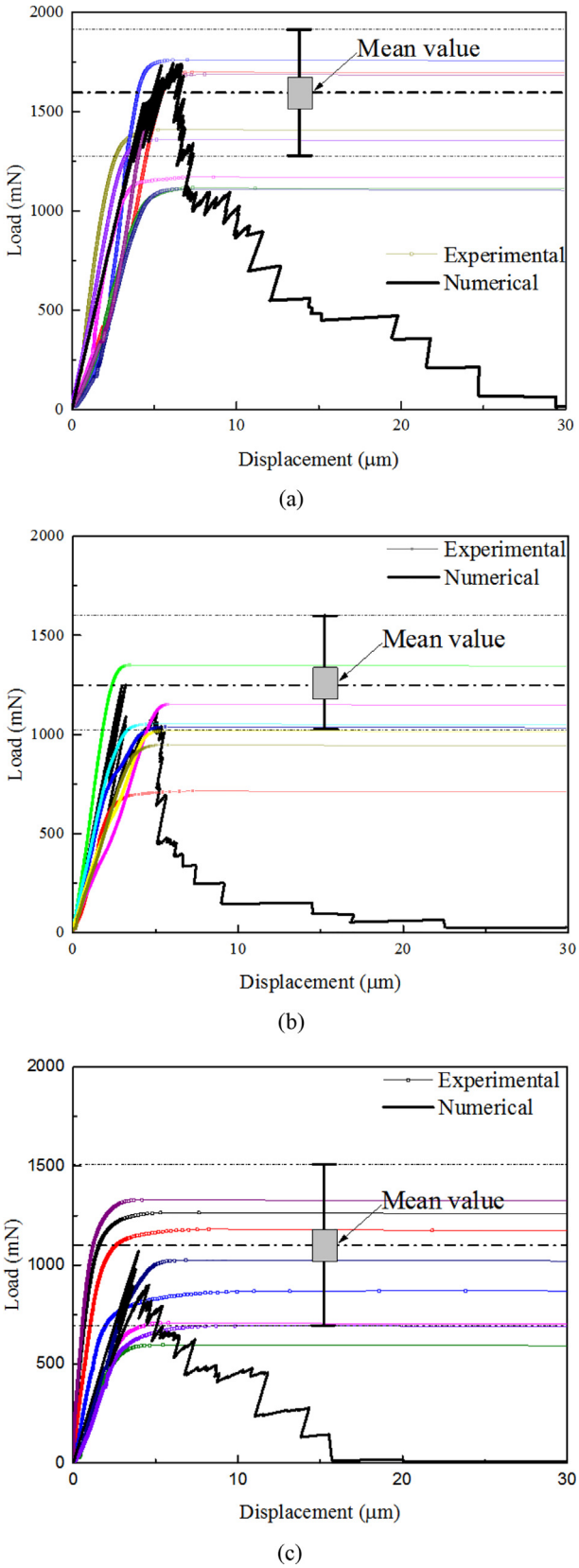

Fig. 15. Comparison of simulated results of 100 μm-sized cubes (with 20 μm AL) with experimental measured results: (a) w/c = 0.3; (b) w/c = 0.4; (b) w/c = 0.5.

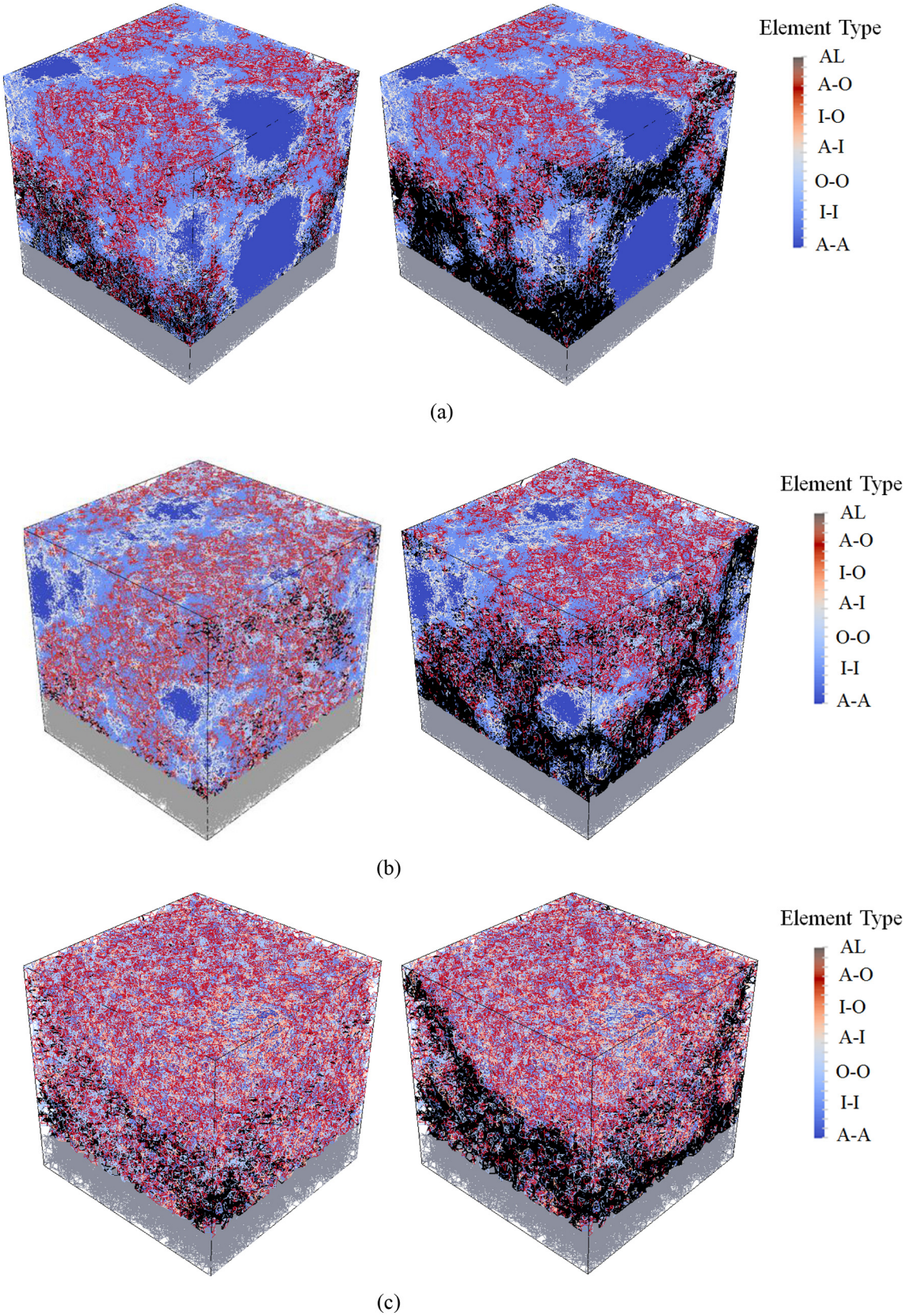

Fig. 16. Simulated crack pattern of 100 μm-sized HCP cubes consisting of AL with w/c ratio (a) 0.3, (b) 0.4 and (c) 0.5 at two stages (left: peak load; right: final failure state, black denotes the crack).

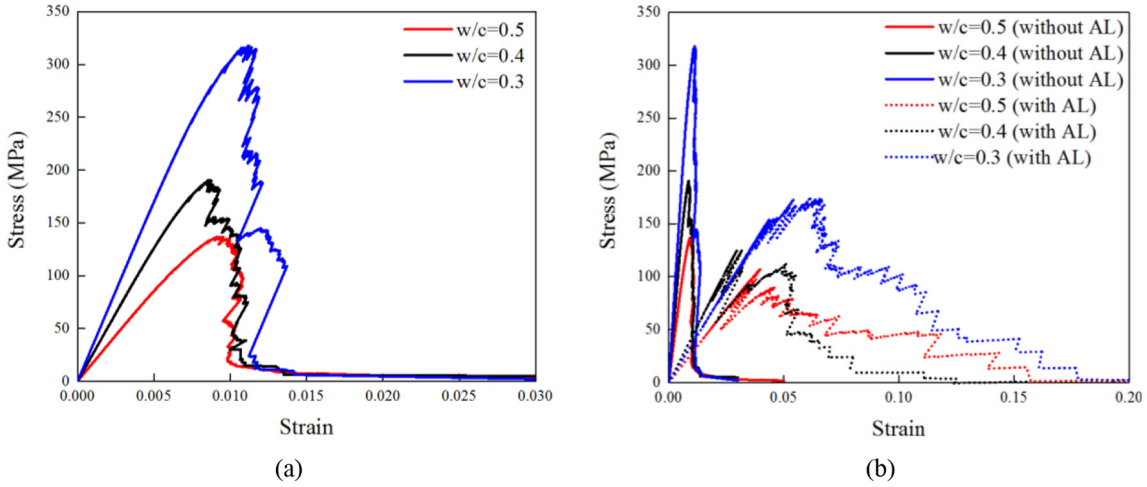

Fig. 17. (a) Simulated stress-strain diagrams of 100 μm-sized HCP cube (without AL) with various w/c ratios; (b) comparison between stress-strain diagrams of 100 μm-sized HCP cube with and without AL.

materials, the Chi-square test does not reject the null hypothesis (the sample data comes from the tested distribution with determined parameters) at 5% significance level, which indicates that both distributions can be applied for the compressive strength and the elastic modulus. However, different p values are found. p is the probability of observing a test statistic as extreme as, or more extreme than, the observed value under the null hypothesis. It is a scalar value in the range [0, 1] and small values of p cast doubt on the validity of the null hypothesis. By comprising p value, it is suggested that the normal distribution is superior to Weibull distribution for the elastic modulus, while the opposite is found for the compressive strength. This is expected, as the elastic modulus is more influenced by the properties of material components and their relative amounts, while the (fracture) strength is also governed by the weakest link in the system.

The mechanical properties of HCP with size of a few hundred micrometres have been rarely measured by experiments. To the best knowledge of the authors, it is the first time that the compressive strength of HCP with such size is tested. Compared with the macroscopic compressive strength of such material or normal concrete [50], the strength measured at the microscale is significantly higher. Even for the specimen prepared with high w/c ratio (i.e. 0.5), a mean value of 110.24 MPa was measured. Likewise, similar trend has been found in terms of the splitting tensile strength measured by the authors [7]. This is mainly because of the fact the micro-scale sized samples are free from air voids or defects larger than the sample size, which creates more stress concentration spots, thus significantly reducing its material strength [2,51,52]. On the other hand, a large scatter is observed as a result of the heterogeneity of such material and small volume of material sampled. Recently, Shahrin et al. [9] has prepared micro-pillar of C-S-H specimens (around a few micrometres) using FIB technique and measured their compressive strengths. The measured compressive strength of 10C-S-H specimens varies from 225 MPa to 606 MPa. As expected, the measured strength from smaller scale shows higher value and a lager variation compared with current work. However, in their work, a sphero-conical indenter is mounted on the nanoindenter to apply the load on the top of the micro-pillar. Consequentially, some of the compressed micro-pillars are split in half, thus the measurements failed to provide the uniaxial compressive strength but a combination of the splitting and compression. Therefore, a somewhat lower value of the C-S-H strength is obtained in their work compared with the assumptions in the current work, where low and high hydration products have a compressive strength of 580 MPa and 920 MPa, respectively (see Table 2).

Furthermore, it is important to notice that the splitting strengths for the same size specimens measured by the authors [7] are 21.28 MPa, 18.72 MPa and 16.5 MPa for w/c ratio 0.3, 0.4 and 0.5, which is around one-eighth of the compressive strength. Considering that the splitting strength is generally about 1.1–1.2 time higher than the uniaxial tensile strength, it is estimated that the uniaxial compressive strength is around 10 times of the uniaxial tensile strength at this scale. This is in accordance with the centimetre sized concrete specimens [50].

Based on the multi-scale modelling, Hlobil et al. [5] give an estimation of compressive strength of HCP at 28 days with w/c ratio 0.297, which equals 147.985 MPa; for w/c ratio 0.51, its compressive strength is estimated as 52.119 MPa. The former prediction is close to the mean value and the latter approximates the lower bound of the current measurements. It is therefore advised that for the mechanical properties of HCP at smaller scale, stochastic results are needed rather than the deterministic results due to the heterogeneous material structure. On the other hand, Pichler et al. [3] calculated the deviatoric strength of a representative volume element of HCP composite with size of 0.7 mm. In order to make their results comparable with the current study, the hydration degree presented in Table 1 was used. It is estimated that, for w/c ratio 0.5, HCP with hydration degree of 0.8 has a compressive strength of 37.5 MPa, while the compressive of HCP with w/c ratio 0.35 and hydration degree of 0.6 is calculated as 60 MPa. Their prediction is much lower compared with the current results, suggesting that a strong size effect probably exists for such a heterogeneous material. The calculated elastic moduli of 100 μm-sized HCP cubes using Eq. (3) are compared with available data in the literature [3,18,53–56], as shown in Fig. 14. The reported moduli in the current work are comparable with the results presented in the literature, but seem relatively lower. This mainly attributes to the fact that the deformation of the substrate material is not considered.

It is worth mentioning that the reported compressive strength in the current work is limited under a loading rate of 10 mN/s. As reported in [57,58], the loading rate has considerable influence on the measured strength, it is therefore expected that various loading rates would be carried out in the further to quantify this loading rate-compressive strength relationship at the micrometre length scale. Additionally, both linear and nonlinear creep behaviours have been observed for the compression test of concrete [59,60] and cement paste [61,62], which have a considerable influence on the failure of the tested material. A nonlinear creep model combined with an ultimate strain criterion has been proposed by Fischer et al. [62] to explain the relationship between the measured strength of 2-day-old cement paste specimens and loading rate. Furthermore, as reported in [61], modulus derived from the stress-stain curve, even at a small stress level is strain rate dependent which is related to the dissipative phenomena. With respect to the micrometre length scale, the influence of creep on the nanoindentation test has been

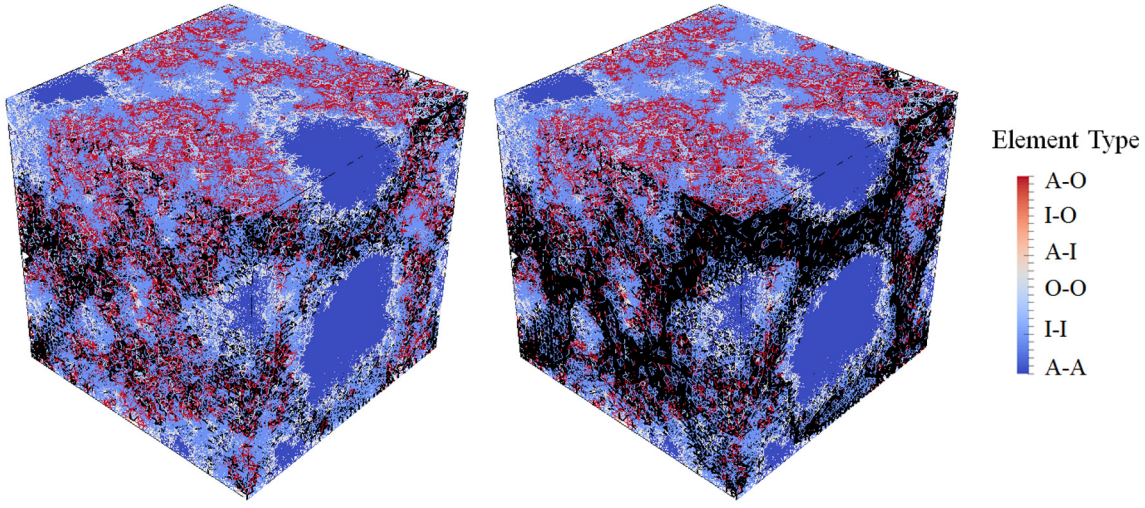

(a)

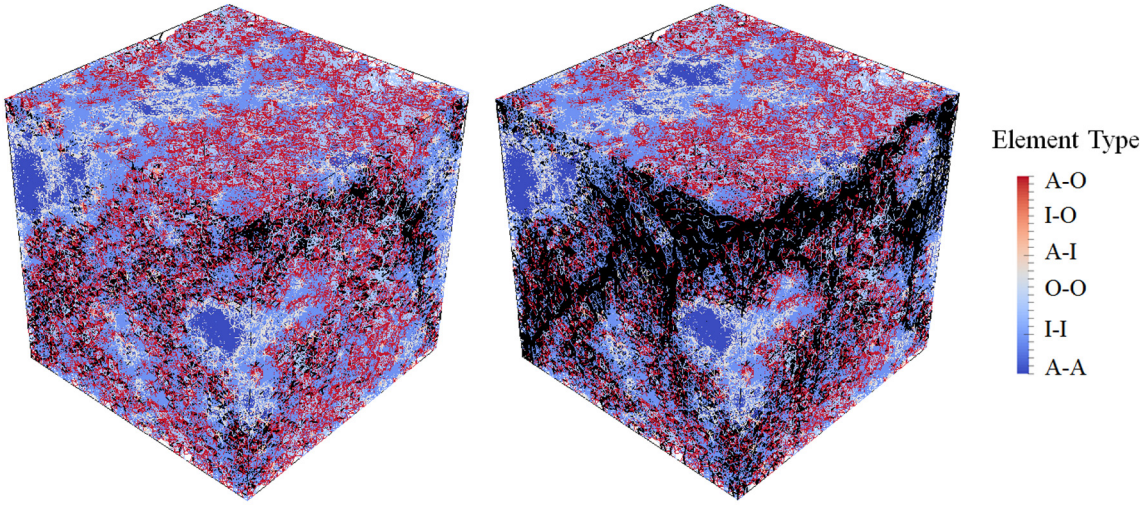

(b)

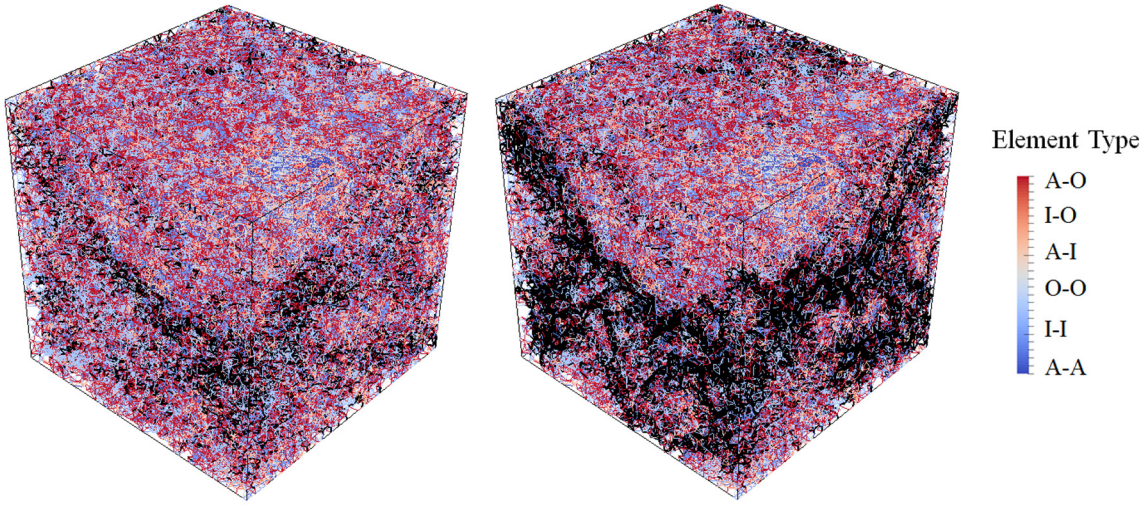

(c)

Fig. 18. Simulated crack pattern of 100 μm-sized HCP cubes with w/c ratio (a) 0.3, (b) 0.4 and (c) 0.5 at two stages (left: peak load; right: final failure state. Black denotes the crack) when no AL is considered.

Table 3
Summary of test results of each type specimen (values in parentheses represent coefficient of variation).

W/c ratio	Quantity	Sample size (μm^3)	Young's modulus (GPa)	Compressive strength (MPa)
0.3	131	100 × 100 × 100	22.21 (0.15)	159.52 (0.20)
	113	200 × 200 × 200	21.81 (0.19)	124.79 (0.13)
	105	400 × 200 × 200	20.34 (0.19)	107.05 (0.20)
0.4	125	100 × 100 × 100	17.16 (0.17)	124.97 (0.28)
	111	200 × 200 × 200	16.95 (0.20)	112.40 (0.20)
	104	400 × 200 × 200	16.53 (0.19)	99.79 (0.31)
0.5	106	100 × 100 × 100	14.34 (0.26)	110.24 (0.37)
	176	200 × 200 × 200	13.78 (0.23)	103.19 (0.32)
	111	400 × 200 × 200	13.31 (0.25)	76.71 (0.32)

Table 4
Fitting results of normal distribution.

W/c ratio	Data sample	μ	s	p
0.3	Elastic modulus	22.21	3.33	0.29
	Compressive strength	159.52	31.82	0.19
0.4	Elastic modulus	17.16	2.90	0.57
	Compressive strength	124.97	34.70	0.75
0.5	Elastic modulus	14.34	3.78	0.32
	Compressive strength	110.24	40.23	0.10

Table 5
Fitting results of Weibull distribution.

W/c ratio	Data sample	η	m	p
0.3	Elastic modulus	23.66	7.44	0.23
	Compressive strength	172.13	5.98	0.30
0.4	Elastic modulus	18.39	6.46	0.35
	Compressive strength	137.93	4.08	0.79
0.5	Elastic modulus	15.76	4.25	0.30
	Compressive strength	123.30	3.27	0.14

Table 6
Comparison between the modelling and experimental results for the specimens with AL (values in parentheses represent coefficient of variation).

W/c ratio	Young's modulus (GPa)		Compressive strength (MPa)	
	Modelling	Experimental	Modelling	Experimental
0.3	29.33	22.21 (0.15)	174.04	159.52 (0.20)
0.4	24.17	17.16 (0.28)	125.09	124.97 (0.28)
0.5	12.32	14.34 (0.26)	107.12	110.24 (0.37)

studied by applying multiple loading cycles on the cement paste [63]. As a sharp tip (Berkovich tip) was used in the test, a high stress concentration occurs below the indenter during the test, leading to a significant creep strain. The magnitude of creep in concrete has been found to be proportional to the intensity of applied stress [50]. A stress concentration occurring underneath a Berkovich indenter should, accordingly, result in high local creep. In uniaxial compression, as tested herein, it is expected that the creep is less pronounced, and is therefore not considered herein. Nevertheless, there is a need for quantifying this effect. This will form a part of a future study.

4.2. Modelling results and discussion

In order to validate the adopted discrete lattice model, the computational uniaxial compression test was first conducted on the virtual specimens containing AL which is comparable with the experimental set up. In Fig. 15, the simulated load-displacement curve is compared with the experiments for each w/c ratio. Clearly, a descending branch after the peak load is obtained from the modelling. However, such post-peak behaviour cannot be captured by the experimental measuring as the test is run under a load control model. Consequently, a load plateau is observed as a result of the overshoot of the indenter. Therefore, the comparison is limited to the pre-peak regime from which the compressive strength and elastic modulus are obtained. It is observed that the slope and peak load from the model are in the range of the experiments, although dispersion remains in the experimental measurements. The calculated strengths and Young's moduli using Eq. (3) are listed in Table 6 and compared with the experimental measured results. Clearly, the simulated Young's moduli are somewhat higher than the measured average values for higher w/c ratios (0.3 and 0.4), while it is lower for the w/c = 0.5. In terms of the strength, the simulated result for w/c ratio = 0.3 is somewhat higher than the measured value, while they correspond quite well for the w/c ratios 0.4 and 0.5. The discrepancy could be attributed to the selected microstructure which is possibly stronger than the average. Due to the heterogeneous nature of the HCP microstructure, it is recommended to study the micro-mechanical properties of HCP in a stochastic way. However, it was not done in the current work, as it requires significant computational efforts. Nevertheless, the simulated results show reasonable agreement with the experimental data. Fig. 16 presents the simulated crack pattern of 100 μm-sized HPC cube consisting AL at stage of peak load and failure for each w/c ratio. It is evident that diagonal main cracks form at the side of the cube at the final crack stage, which agrees with the experimental observations. The comparison proves that the adopted discrete lattice model can simulate the conducted experimental compressive measurement and give a reasonable prediction in terms of the compressive strength and elastic modulus.

After validation, the compressive fracture performance of HCP was modelled using the 100 μm-sized virtual cubes without the AL. The used local mechanical properties of lattice element remain unchanged as aforementioned. Herein, a high friction compression boundary condition was applied by restraining deformation of horizontal displacement of the nodes at two ends. Fig. 17 presents the simulated stress-strain curve of HCP cube with different w/c ratios. The elastic modulus and compressive strength were derived from the stress-strain curve and listed in Table 7 together with the tensile strength that obtained by the authors from exactly same virtual specimens [16]. As expected, HCP with lower w/c ratio has a higher strength and elastic modulus. The ratio of compressive/tensile strength ranges from 7.91 to 9.66, which is in accordance with concrete [1]. Compared with the results (for both simulations and measurements) with adhesive layer, somewhat higher strengths and moduli are obtained for all w/c ratios once the AL is removed. This is attributed to relatively low stiffness of AL which reduces the ability to restrain the deformation of the bottom surface of HPC. Furthermore, it is worth mentioning that Eq. (3) does not consider the deformation of the substrate glass and the possible creep of the micro-cubes, which results in an underestimation of the realistic Young's modulus. Nevertheless, the numerical and experimental results

Table 7
Calculated global mechanical properties, compared with tensile strength in the literature [16].

W/c ratio	Young's modulus (GPa)	Compressive strength (MPa)	Tensile strength (MPa) [16]	Compressive strength/tensile strength
0.3	33.27	317.72	32.9	9.66
0.4	25.40	190.52	22.3	8.54
0.5	16.97	136.81	17.3	7.91

are in the same order. As the modelling can simulate the fracture behaviour of material under ideal boundary conditions which cannot be achieved by the current experimental techniques, it is more plausible to up-scale of the simulated strengths and Young's moduli for the meso-scale analysis. As shown in Fig. 18, the simulated fracture patterns at peak load and the final failure stages are presented. Typical inclined fracture pattern is observed more pronounced in the HPC cube prepared with higher w/c ratio, in which fewer stiff inclusions, i.e. anhydrous cement particles remain in the microstructure. As these inclined cracks are distributed by the anhydrous cement particles leading to more crack branches and stable crack propagation, the cement paste with lower w/c ratio has a higher load bearing capacity (higher strength).

In the end, it is worth mentioning that, for each w/c ratio, only one virtual specimen was tested using the developed discrete model. To have a more comprehensive understanding of compressive failure of HPC at the micrometre length scale, more virtual specimens need to be created and tested like Ref. [7, 29] to have a stochastic-based results. Furthermore, the influence of the size and shape of specimens on their fracture performance as listed in Table 3 should also be investigated using the developed model following the approach as discussed in [2,64]. However, compared with the computational uniaxial test, the compression test requires significantly more computational time as compressive failure process is more complex and more (micro) cracks form before the specimen fails. It is expected that the mentioned limitations would be overcome with more power computational facilities and a more efficient numerical algorithm in the future.

5. Conclusions

In the current work, a new approach has been developed to study the compressive failure of micrometre sized HCP specimens. This approach involves sample preparation using thin-section, polishing and micro-dicing, and compression test using nanoindenter. Besides, a microstructure informed discrete lattice model was used to mimic the failure process of specimens under compression. Although a stable measuring of post-peak stage is missing in the experiments because of the limitation of instruments, a reasonable agreement between modelling (considering the AL) and experiment is found in the pre-peak stage in terms of the load-displacement curve and crack pattern. Based on the current study, the following conclusions can be drawn:

- Although slenderness and w/c ratio play a significant role on the compressive fracture performance of HCP, the experimental measured strength in this work is much higher than the strength measured from centimetre sized specimens and lower than the one for smaller sized specimens.
- The Chi-square goodness-of-fit test shows that both normal distribution and Weibull distribution are applicable to describe the experimental probability distribution of compressive strength and elastic modulus. While the normal distribution is more suitable for the elastic modulus and Weibull distribution is better for the compressive strength.
- The input local mechanical properties for the discrete lattice model are calibrated from the authors' previous work, and results in satisfactory modelling results when compared with the experimental measurements. Together with the authors' previous publications [16], the lattice model is capable of simulating both tensile and compressive fracture behaviours of HCP at the micrometre length scale, which forms the basis for the multi-scale modelling of cementitious material.
- From both modelling and testing, the compressive strength is almost 10 times of the tensile strength which is in accordance with the phenomenon that observed for the centimetre sized concrete specimens.

In the end, it is important to notice the limitations of the current experimental set up. First, the influence of AL and substrate underneath the HCP on the measured displacement is not considered. Thus, the estimated elastic modulus based on the linear elastic assumption is relatively low. This is expected to be solved by monitoring the deformation at two ends of HCP using a high magnification camera during the mechanical test. The other is that the stable post-peak cannot be captured by the nanoindenter. Therefore, a more advanced instrument with adequate high-resolution system for displacement control and measurements is needed.

Declaration of competing interest

The authors declare that they have no known competing financial interests or personal relationships that could have appeared to influence the work reported in this paper.

Acknowledgements

Hongzhi Zhang, Yading Xu, Yidong Gan and Ze Chang would like to acknowledge the funding supported by China Scholarship Council under grant number 201506120067, 201708110187, 201706130140 and 201806060129 respectively. The authors would also like to acknowledge the help of Mr. Arjan Thijssen with XCT and ESEM experiments.

References

[1] J.G. Van Mier, Concrete Fracture: A Multiscale Approach, CRC Press, 2012.
[2] H. Zhang, B. Šavija, Y. Xu, E. Schlangen, Size effect on splitting strength of hardened cement paste: experimental and numerical study, Cem. Concr. Compos. 94 (2018) 264–276.
[3] B. Pichler, C. Hellmich, Upscaling quasi-brittle strength of cement paste and mortar: a multi-scale engineering mechanics model, Cem. Concr. Res. 41 (2011) 467–476.
[4] B. Pichler, C. Hellmich, J. Eberhardsteiner, J. Wasserbauer, P. Termkhajornkit, R. Barbarulo, G. Chanvillard, Effect of gel–space ratio and microstructure on strength of hydrating cementitious materials: an engineering micromechanics approach, Cem. Concr. Res. 45 (2013) 55–68.
[5] M. Hlobil, V. Šmilauer, G. Chanvillard, Micromechanical multiscale fracture model for compressive strength of blended cement pastes, Cem. Concr. Res. 83 (2016) 188–202.
[6] S. Harsh, Z. Shen, D. Darwin, Strain-Rate Sensitive Behavior of Cement Paste and Mortar in Compression, American Concrete Institute, 1990.
[7] H. Zhang, B. Šavija, E. Schlangen, Combined experimental and numerical study on micro-cube indentation splitting test of cement paste, Eng. Fract. Mech. 199 (2018) 773–786.
[8] D. Larson, D. Foord, A. Petford-Long, H. Liew, M. Blamire, A. Cerezo, G. Smith, Field-ion specimen preparation using focused ion-beam milling, Ultmi 79 (1999) 287–293.
[9] R. Shahrin, C.P. Bobko, Characterizing strength and failure of calcium silicate hydrate aggregates in cement paste under micropillar compression, J. Nanomech. Micromech. 7 (2017) 06017002.
[10] J. Němeček, V. Králík, V. Šmilauer, L. Polívka, A. Jäger, Tensile strength of hydrated cement paste phases assessed by micro-bending tests and nanoindentation, Cem. Concr. Compos. 73 (2016) 164–173.
[11] S.J. Chen, W.H. Duan, Z.J. Li, T.B. Sui, New approach for characterisation of mechanical properties of cement paste at micrometre scale, Mater. Des. 87 (2015) 992–995.
[12] M. Nikolić, E. Karavelić, A. Ibrahimbegovic, P. Miščević, Lattice element models and their peculiarities, Archives Comput. Methods Eng. (2017) 1–32.
[13] Z. Pan, R. Ma, D. Wang, A. Chen, A review of lattice type model in fracture mechanics: theory, applications, and perspectives, Eng. Fract. Mech. 190 (2018) 382–409.
[14] G. Lilliu, J.G. van Mier, 3D lattice type fracture model for concrete, Eng. Fract. Mech. 70 (2003) 927–941.
[15] E. Schlangen, E. Garboczi, Fracture simulations of concrete using lattice models: computational aspects, Eng. Fract. Mech. 57 (1997) 319–332.
[16] H. Zhang, B. Šavija, S. Chaves Figueiredo, M. Lukovic, E. Schlangen, Microscale testing and modelling of cement paste as basis for multi-scale modelling, Materials 9 (2016) 907.
[17] L.-Y. Lv, H. Zhang, E. Schlangen, Z. Yang, F. Xing, Experimental and numerical study of crack behaviour for capsule-based self-healing cementitious materials, Constr. Build. Mater. 156 (2017) 219–229.
[18] G. Constantinides, F.-J. Ulm, The effect of two types of CSH on the elasticity of cement-based materials: results from nanoindentation and micromechanical modeling, Cem. Concr. Res. 34 (2004) 67–80.
[19] C. Hu, Z. Li, Micromechanical investigation of Portland cement paste, Constr. Build. Mater. 71 (2014) 44–52.

[20] K. Van Breugel, Numerical simulation of hydration and microstructural development in hardening cement-based materials:(II) applications, Cem. Concr. Res. 25 (1995) 522–530.
[21] S. Bishnoi, K.L. Scrivener, μic: a new platform for modelling the hydration of cements, Cem. Concr. Res. 39 (2009) 266–274.
[22] D.P. Bentz, D.P. Bentz, CEMHYD3D: A Three-Dimensional Cement Hydration and Microstructure Development Modelling Package, Version 2.0 US Department of Commerce, National Institute of Standards and Technology, 2000.
[23] T. Chotard, M. Boncoeur-Martel, A. Smith, J. Dupuy, C. Gault, Application of X-ray computed tomography to characterise the early hydration of calcium aluminate cement, Cem. Concr. Compos. 25 (2003) 145–152.
[24] M. Zhang, Y. He, G. Ye, D.A. Lange, K. van Breugel, Computational investigation on mass diffusivity in Portland cement paste based on X-ray computed microtomography (μCT) image, Constr. Build. Mater. 27 (2012) 472–481.
[25] T.-S. Han, X. Zhang, J.-S. Kim, S.-Y. Chung, J.-H. Lim, C. Linder, Area of lineal-path function for describing the pore microstructures of cement paste and their relations to the mechanical properties simulated from μ-CT microstructures, Cem. Concr. Compos. 89 (2018) 1–17.
[26] X. Feng, E.J. Garboczi, D.P. Bentz, P.E. Stutzman, T.O. Mason, Estimation of the degree of hydration of blended cement pastes by a scanning electron microscope point-counting procedure, Cem. Concr. Res. 34 (2004) 1787–1793.
[27] K.L. Scrivener, Backscattered electron imaging of cementitious microstructures: understanding and quantification, Cem. Concr. Compos. 26 (2004) 935–945.
[28] J. Zhang, G.W. Scherer, Comparison of methods for arresting hydration of cement, Cem. Concr. Res. 41 (2011) 1024–1036.
[29] H. Zhang, B. Šavija, E. Schlangen, Towards understanding stochastic fracture performance of cement paste at micro length scale based on numerical simulation, Constr. Build. Mater. 183 (2018) 189–201.
[30] B. Šavija, G.E. Smith, P.J. Heard, E. Sarakinou, J.E. Darnbrough, K.R. Hallam, E. Schlangen, P.E. Flewitt, Modelling deformation and fracture of Gilsocarbon graphite subject to service environments, JNuM 499 (2017) 18–28.
[31] B. Šavija, D. Liu, G. Smith, K.R. Hallam, E. Schlangen, P.E. Flewitt, Experimentally informed multi-scale modelling of mechanical properties of quasi-brittle nuclear graphite, Eng. Fract. Mech. 153 (2016) 360–377.
[32] Z. Qian, Multiscale Modeling of Fracture Processes in Cementitious Materials, Delft University of Technology, Delft, The Netherlands, 2012.
[33] H.J. Herrmann, A. Hansen, S. Roux, Fracture of disordered, elastic lattices in two dimensions, PhRvB 39 (1989) 637.
[34] H. Zhang, B. Šavija, M. Luković, E. Schlangen, Experimentally informed micromechanical modelling of cement paste: an approach coupling X-ray computed tomography and statistical nanoindentation, Compos. Part B 157 (2019) 109–122.
[35] M. Yip, J. Mohle, J. Bolander, Automated modeling of three-dimensional structural components using irregular lattices, Comput-Aided Civ. Inf. 20 (2005) 393–407.
[36] E. Schlangen, J.G.M. Van Mier, Simple lattice model for numerical simulation of fracture of concrete materials and structures, Eng. Fract. Mech. 25 (9) (1992) 534–542.
[37] Z. Qian, E. Schlangen, G. Ye, K. van Breugel, Modeling framework for fracture in multiscale cement-based material structures, Materials 10 (2017) 587.
[38] E. Schlangen, Crack development in concrete, part 2: modelling of fracture process, Key Eng. Mater. Trans. Tech. Publ. (2008) 73–76.
[39] M.A. van Vliet, J.M. van Mier, Experimental investigation of concrete fracture under uniaxial compression, Mech. Cohesive-frictional Mater. Int. J. Exp. Model. Comput. Mater. Struct. 1 (1996) 115–127.
[40] M. Abreu, J. Lemos, J. Carmeliet, E. Schlangen, Modelling compressive cracking in concrete by a modified lattice model, Proceedings of the 6th International Conference on Fracture Mechanics of Concrete and Concrete Structures, New Trends in Fracture Mechanics of Concrete, 2007, pp. 453–460.
[41] K.H. Gerstle, D.L. Linse, P. Bertacchi, Strength of concrete under multiaxial stress states, Special Publication 55 (1978) 103–132.
[42] M. Kotsovos, Effect of testing techniques on the post-ultimate behaviour of concrete in compression, Mater. Constr. 16 (1983) 3–12.
[43] J.G.M. Van Mier, Strain-softening of Concrete Under Multiaxial Loading Conditions, Eindhoven University of Technology, Eindhoven, The Netherlands, 1984.
[44] P. Tumidajski, L. Fiore, T. Khodabocus, M. Lachemi, R. Pari, Comparison of Weibull and normal distributions for concrete compressive strengths, CaJCE 33 (2006) 1287–1292.
[45] F.W. Zok, On weakest link theory and Weibull statistics, J. Am. Ceram. Soc. 100 (2017) 1265–1268.
[46] M.R. Van Vliet, J.G. Van Mier, Experimental investigation of size effect in concrete and sandstone under uniaxial tension, Eng. Fract. Mech. 65 (2000) 165–188.
[47] T.-f. Wong, R.H. Wong, K. Chau, C. Tang, Microcrack statistics, Weibull distribution and micromechanical modeling of compressive failure in rock, Mech. Mater. 38 (2006) 664–681.
[48] J.B. Quinn, G.D. Quinn, A practical and systematic review of Weibull statistics for reporting strengths of dental materials, Dent. Mater. 26 (2010) 135–147.
[49] W.G. Cochran, The χ^2 test of goodness of fit, Ann. Math. Stat. (1952) 315–345.
[50] P.K. Mehta, P.J. Monteiro, Concrete Microstructure, Properties and Materials, (2017).
[51] D. Liu, B. Šavija, G.E. Smith, P.E. Flewitt, T. Lowe, E. Schlangen, Towards understanding the influence of porosity on mechanical and fracture behaviour of quasi-brittle materials: experiments and modelling, Int. J. Fract. (2017) 1–16.
[52] D. Liu, K. Mingard, O.T. Lord, P. Flewitt, On the damage and fracture of nuclear graphite at multiple length-scales, JNuM 493 (2017) 246–254.
[53] C.-J. Haecker, E. Garboczi, J. Bullard, R. Bohn, Z. Sun, S. Shah, T. Voigt, Modeling the linear elastic properties of Portland cement paste, Cem. Concr. Res. 35 (2005) 1948–1960.
[54] J. Sanahuja, L. Dormieux, G. Chanvillard, Modelling elasticity of a hydrating cement paste, Cem. Concr. Res. 37 (2007) 1427–1439.
[55] O. Bernard, F.-J. Ulm, E. Lemarchand, A multiscale micromechanics-hydration model for the early-age elastic properties of cement-based materials, Cem. Concr. Res. 33 (2003) 1293–1309.
[56] M. Zhang, A.P. Jivkov, Micromechanical modelling of deformation and fracture of hydrating cement paste using X-ray computed tomography characterisation, Compos. Part B 88 (2016) 64–72.
[57] H. Fu, M. Erki, M. Seckin, Review of effects of loading rate on concrete in compression, J. Struct. Eng. 117 (1991) 3645–3659.
[58] Z.P. Bažant, R. Gettu, Rate effects and load relaxation in static fracture of concrete, ACI Mater. J. 89 (1992) 456–468.
[59] C. Mazzotti, M. Savoia, Nonlinear creep damage model for concrete under uniaxial compression, J. Eng. Mech. 129 (2003) 1065–1075.
[60] M.F. Ruiz, A. Muttoni, P.G. Gambarova, Relationship between nonlinear creep and cracking of concrete under uniaxial compression, J. Adv. Concr. Technol. 5 (2007) 383–393.
[61] M. Irfan-ul-Hassan, B. Pichler, R. Reihsner, C. Hellmich, Elastic and creep properties of young cement paste, as determined from hourly repeated minute-long quasi-static tests, Cem. Concr. Res. 82 (2016) 36–49.
[62] I. Fischer, B. Pichler, E. Lach, C. Terner, E. Barraud, F. Britz, Compressive strength of cement paste as a function of loading rate: experiments and engineering mechanics analysis, Cem. Concr. Res. 58 (2014) 186–200.
[63] J. Němeček, Creep effects in nanoindentation of hydrated phases of cement pastes, Mater. Charact. 60 (2009) 1028–1034.
[64] G. Cusatis, A. Mencarelli, D. Pelessone, J. Baylot, Lattice discrete particle model (LDPM) for failure behavior of concrete. II: calibration and validation, Cem. Concr. Compos. 33 (2011) 891–905.